buildings

Article

Study on the Performance Evolution of Hydraulic Concrete under the Alternating Action of Freeze–Thaw and Abrasion

Baoguo Wu [1,2], Shuangxi Li [1,2,*] and Chunmeng Jiang [1,2]

1 College of Water and Civil Engineering, Xinjiang Agricultural University, Urumqi 830052, China; xjwubg@163.com (B.W.); jiangcm93@163.com (C.J.)
2 Xinjiang Key Laboratory of Hydraulic Engineering Security and Water Disasters Prevention, Urumqi 830052, China
* Correspondence: xjlisx123@xjau.edu.cn

Abstract: The hydraulic concrete in the alpine region is subjected to alternating actions of freeze–thaw (F) and abrasion (W) during operation, resulting in significant deterioration of concrete durability. In this paper, the water/binder ratio (W/B) was employed as the test variable, the working condition F group and W group were set as the control group, and the working condition F-W group was used as the test group. Fast-freezing and underwater methods are used for the alternating test. By measuring the mass loss, relative dynamic elastic modulus (RDEM), surface morphological characteristics, fractal dimension of concrete in each alternating cycle, and the evolution law of concrete performance under the alternating action of F and W was explored. The results show that compared with the control group, the alternating action will accelerate the mass loss of concrete, reduce the RDEM, and cause the deterioration of surface wear. The maximum increase in mass loss and RDEM of concrete is 1.92% and 20.11%, respectively. During this process, the fractal dimension of the concrete increases as the number of alternating cycles increases, but it still does not exceed the limit of 2.4. In addition, a relationship function between the fractal dimension and the mass loss rate, volume loss, was established. It was found that the experimental group had a good linear correlation, and the correlation was close to 95%, which was about 20% higher than that of the control group.

Keywords: hydraulic concrete; freeze–thaw; abrasion; surface morphology indexes; fractal dimension

Citation: Wu, B.; Li, S.; Jiang, C. Study on the Performance Evolution of Hydraulic Concrete under the Alternating Action of Freeze–Thaw and Abrasion. *Buildings* **2024**, *14*, 1369. https://doi.org/10.3390/buildings14051369

Academic Editor: Grzegorz Ludwik Golewski

Received: 15 April 2024
Revised: 3 May 2024
Accepted: 7 May 2024
Published: 10 May 2024

1. Introduction

As a kind of building material with many excellent characteristics, concrete is applied to the construction of hydraulic structures [1]. Hydraulic structures are exposed to complex and polytropic unfavourable operating environments during their operation. The performance degradation and damage of bridge materials are more extensive in hot regions, although these are accidental accidents [2–5]. The durability of concrete in cold regions is affected by freeze–thaw and abrasion damage, which can pose a challenge to the stability of the hydrostructure [6]. The temperature varies greatly during the spring and winter, and hydraulic concrete across rivers in this area suffers frequent freeze–thaw damage [7]. At the same time, hydraulic concrete is inevitably subjected to the impact and friction of sand-carrying rivers for a long time [8,9]. Especially during the summer and autumn, hydraulic concrete is subjected to extremely severe abrasion damage caused by bed load. In the actual service environment, these hydraulic structures are exposed to the repeated alternation of freeze–thaw and abrasion, which can lead to deterioration. It is found that the degree of alternating damage is greater than that of single damage [10,11].

Currently, the majority of the existing research is devoted to the influence of a single factor on the performance of hydraulic concrete, while research under the action of multiple factors is relatively scarce [12]. For example, the addition of an appropriate amount of fibre into pervious concrete can enhance its resistance to wear while enhancing permeability by modifying the structural framework of concrete, thereby reducing the erosion damage inflicted by high-speed water flow [13–15]. The coupling of freeze–thaw cycles and adverse effects on hydraulic structures is the main focus of this type of multi-factor study [16–21]. Concerning the problem of the abrasion damage of concrete under freeze–thaw conditions, the existing studies mainly consider the abrasion problem generated by ice and the mechanical abrasion phenomenon of deicer on airport runways, while the performance evolution law of the alternating effects of freeze–thaw cycles and abrasion damage is not clear [22–25]. Research into hydraulic concrete in cold regions is therefore urgently needed.

The underwater method is a frequently employed experimental approach that is utilised to simulate the deterioration of concrete by bed load [26]. The mass loss rate and abrasion resistance strength are employed as indexes to assess the abrasion resistance of concrete. However, these two indicators cannot effectively characterise the process of concrete damage from the surface to the interior during operation. At present, certain scholars have introduced the incorporation of morphology and fractal dimension, which encompass a greater range of damage features as a novel approach to assessing the wear resistance of concrete surfaces, yielding promising outcomes. Hasan utilised 3D laser scanning technology to determine the characteristics of volume loss and surface morphology of concrete wear [27]. Sarker confirms that this technique has a better characterisation of concrete wear morphology by comparing it with other quantitative evaluation indexes [28].

In this paper, the water/binder ratio is employed in this investigation as a test variable, with both the fast-freezing and underwater methods utilised for the test. Compared with the working conditions of the F group and W group, the evolution law of the mass loss, RDEM, surface morphology, and fractal dimension of the hydraulic concrete in the working condition F-W group with the number of alternating cycles were studied. The surface morphology of the concrete samples was analysed using the mechanical probe testing point method, which also enabled the calculation of the abrasion depth and volume. Meanwhile, the fractal dimension of the abrasion surface was determined by employing the cube-covering method, with the relationship between the fractal dimension and the mass loss rate and volume loss subsequently established.

2. Materials and Methods

2.1. Materials and Mixture Design

Ordinary Portland cement (P.O 42.5R) was manufactured by Tianshan Mountains Cement Co., Ltd., Urumqi, China, with a specific surface area of 384 m^2/kg, cement density of 3.08 g/cm^3, stability qualified. The test used tap water from Urumqi City, China, with good quality. The coarse aggregate was selected from 5–20 mm continuous graded limestone gravel, with an apparent density of 2646 kg/m^3. The fine aggregate was taken from continuous grading machine-made sand, with an apparent density of 2553 kg/m^3, the fineness modulus of 2.94. The water reducer adopted was polycarboxylate-based High-Range Water Reducer produced by Feike New Material Technology Co., Ltd., Yuncheng City, China, with a water reduction rate of 30%.

According to the Chinese Standard for the Water Conservancy Industry (SL/T352—2020), the water/binder ratio of hydraulic concrete in the upstream and downstream water level change areas and the scoured parts of the water flow is to be maintained at a maximum of 0.45 [29]. A review of the relevant literature reveals that the water/binder ratio is typically set at 0.30, 0.35, or 0.4 [30,31]. In accordance with the specifications for the maximum particle size and slump of the gravel, the initial selection of water consumption is 175 $kg{\cdot}m^{-3}$. When the water/binder ratio is 0.4, considering the fineness modulus of fine aggregate and the coarse and fine aggregate are produced manually, the selected sand ratio is 42%. The sand rate remains unaltered. Subsequently, the preliminary calculation of the hydraulic concrete mix proportion is based on the density of each raw material. The moisture content and water absorption of coarse and fine aggregates are analysed in order to adjust the mix ratio. The adjusted mix ratio of hydraulic concrete is presented in Table 1.

Table 1. Hydraulic concrete mix ratio.

Specimen Number	Water Cement Ratio	Cement/ kg·m^{-3}	Water/ kg·m^{-3}	Sand/ kg·m^{-3}	Stone/ kg·m^{-3}	Water Reducer/%
A1	0.43	387.5	168.4	801	1109.4	0.2
A2	0.38	442.9	167.7	758.7	1050.7	0.2
A3	0.32	516.7	167.3	732.0	1013.7	0.2

The objective is to analyse the deterioration mechanism of water/binder ratio on concrete under the alternating action of freeze–thaw and abrasion. The specimen sizes were unified with a diameter of 300 mm and a height of 100 mm, and freeze–thaw and abrasion tests were carried out. This specimen is a non-standard specimen for the freeze–thaw test, so it is necessary to customise a stainless-steel specimen box with a size of 120 mm × 400 mm × 400 mm for placing the specimen.

2.2. Test Scheme

In this study, three groups of working conditions are designed to analyse the performance evolution under the alternating action of F and W. The various mix ratios correspond to three distinct groups of working conditions, which in turn correspond to three concrete specimens each. This results in a total of nine concrete specimens. The working condition F group is defined as a freeze–thaw cycles group. The specimens were adapted to 50 times, 100 times, 150 times, and 200 freeze–thaw cycles by the fast-freezing method. The mass loss rate, RDEM, and damage layer thickness were tested. The working condition W group is the abrasion damage group. The specimens were adapted to 72 h, 144 h, 216 h, and 288 h of abrasion damage by underwater method. The mass loss rate and 3D surface morphology were tested. The working condition F-W group is the alternating test group, with 'freeze–thaw 50 times + abrasion 72 h' as an alternating cycle. The test was carried out as follows: The specimens were subjected to 50 freeze–thaw cycles by fast-freezing method and then worn by underwater method for 72 h, and the above operation repeated to complete four alternating cycles. The mass loss rate, RDEM, and 3D surface morphology were tested. The main test equipment included: DT-16 dynamic bomb instrument, ZBL-U510 nonmetallic ultrasonic tester, and XG-100 fine rod digital display depth gauge. The test scheme design is shown in Table 2. The test flow chart of three working conditions is shown in Figure 1.

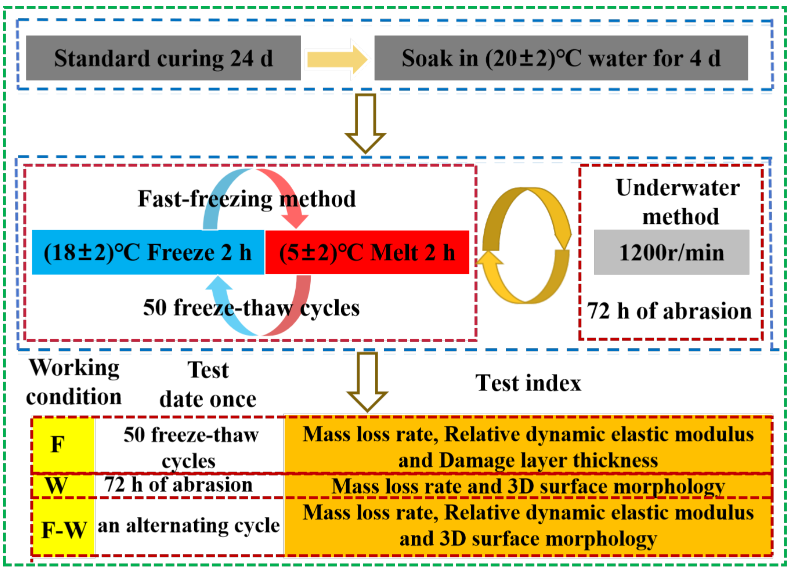

Figure 1. Test flow chart.

Table 2. Test scheme design.

Working Condition	Test Scheme	Test Specimen Number
F	50, 100, 150, and 200 times of freeze–thaw cycles	F-A1, F-A2, F-A3
W	72, 144, 216, and 288 h of abrasion damage	W-A1, W-A2, W-A3
F-W	1, 2, 3, 4 alternating cycles	F-W-A1, F-W-A2, F-W-A3

2.3. Test Methods

2.3.1. Fast-Freezing Test

Based on the Chinese Standard for the Water Conservancy Industry (SL/T352—2020), HDK-5 fast freeze–thaw testing machine was used to carry out frost resistance test [29]. After 28 days of curing, the initial mass and initial transverse frequency of the specimens were tested. The specimens of working condition F group experienced 200 freeze–thaw cycles. The mass, transverse frequency, and ultrasonic velocity were tested at intervals of 50 cycles, and the mass loss rate, RDEM, and damage layer thickness were calculated. The equipment for fast-freezing method test, the placement of concrete specimens, and the test of transverse frequency are shown in Figure 2.

(**a**) (**b**) (**c**)

Figure 2. Fast-freezing test: (**a**) HDK-5 fast freeze-thaw testing machine; (**b**) The placement of concrete specimens; (**c**) Transverse frequency test.

2.3.2. Damage Layer Thickness

The samples were wiped on a saturated dry surface before the testing. The damage thickness layer was tested according to the ultrasonic plane test method in the Chinese Standard for the Engineering Construction Standardization Association (CECS201-2000) [32]. During the test, one side of the specimen with a diameter of 300 mm was selected for the test. The emitter T was positioned at a distance of 50 mm from the surface of the selected sample. From the emitter T, the receiving transducer R was placed at a certain distance along the surface of the sample. The initial distance measurement is 50 mm, followed by successive testing points at intervals of 25 mm, 25 mm, 50 mm, 50 mm, and 50 mm. The coupling agent was Vaseline. The ultrasonic velocity test is shown in Figure 3.

The damage layer can be determined according to the propagation mode of the emitter T and the receiving transducer R ultrasonic wave at different distances [33]. The damage transition layer is used as the dividing line. When the ultrasonic wave passes through the dividing line twice in a certain position range, the position is called the critical point.

$$\frac{l_0}{V_d} = \frac{2\sqrt{h_f^2 + x^2}}{V_d} + \frac{l_0 - 2x}{V_u} \tag{1}$$

The calculation of damage layer thickness (h_f) is as follows:

$$h_f = \frac{l_0}{2}\sqrt{\frac{V_u - V_d}{V_u + V_d}} \tag{2}$$

where the ultrasonic velocity (km/s) of the corresponding layer of concrete is represented by the values V_u and V_d, respectively.

The relationship between the ultrasonic time and the range finding is shown in Figure 4. The intersection point of the two fitting lines in the figure is the change point of ultrasonic time, which is set to (t_0, l_0).

$$l_d = A_d + V_d t_d \tag{3}$$

$$l_u = A_u + V_u t_u \tag{4}$$

where l_d and L_u represent the distance before and after l_0, respectively, t_d and t_u correspond to the sound of the above distance in order, A_d, A_u, V_d, and V_u are the fitting parameters of the functional relationship. The ultrasonic time change point l_0 can be calculated by Equation (5):

$$l_0 = \frac{A_d V_u - A_u V_d}{V_u - V_d} \tag{5}$$

Substituting (5) into Formula (2), the damage layer thickness of concrete can be obtained.

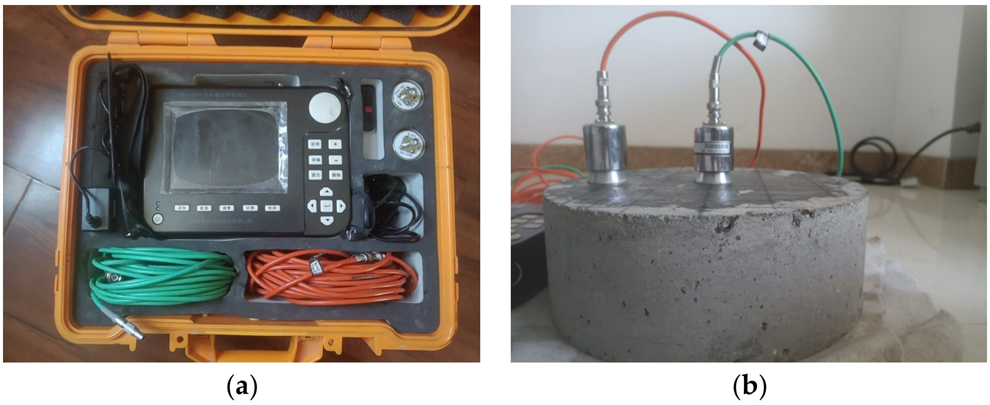

Figure 3. Ultrasonic velocity test: (**a**) ZBL-U510 nonmetallic ultrasonic tester. (**b**) Setting of the transducers.

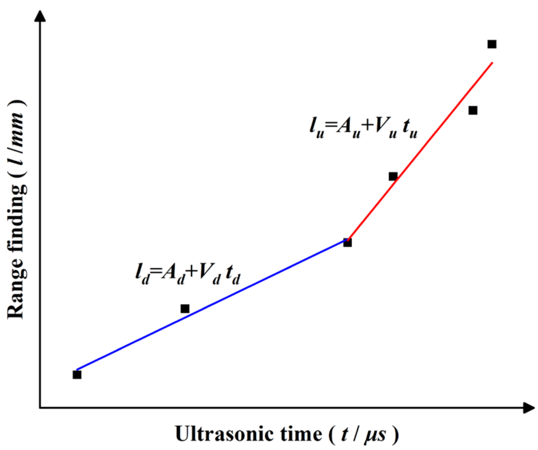

Figure 4. Relationship between the ultrasonic time and the range finding.

2.3.3. Abrasion Test

Based on the Chinese Standard for the Water Conservancy Industry (SL/T352—2020) and ASTM C1138, HKCM-2 abrasion resistance performance testing machine was used to carry out abrasion resistance test [29,34]. After 28 days of curing, the initial mass of the specimens was tested. The specimens of working condition W group experienced 288 h of abrasion damage. The mass and 3D surface morphology were tested at intervals of 72 h, and the mass loss rate and fractal dimension were calculated. The specimens of working condition F-W group experienced 4 alternating cycles. The mass, transverse frequency and 3D surface morphology were tested at intervals of alternating cycles, and the mass loss rate, REDM, and fractal dimension were calculated. The equipment for underwater method test and the placement of steel ball are shown in Figure 5. The rotation speed of the steel stirrer in water was 1200 rpm, which drives the steel ball on the surface of the specimen.

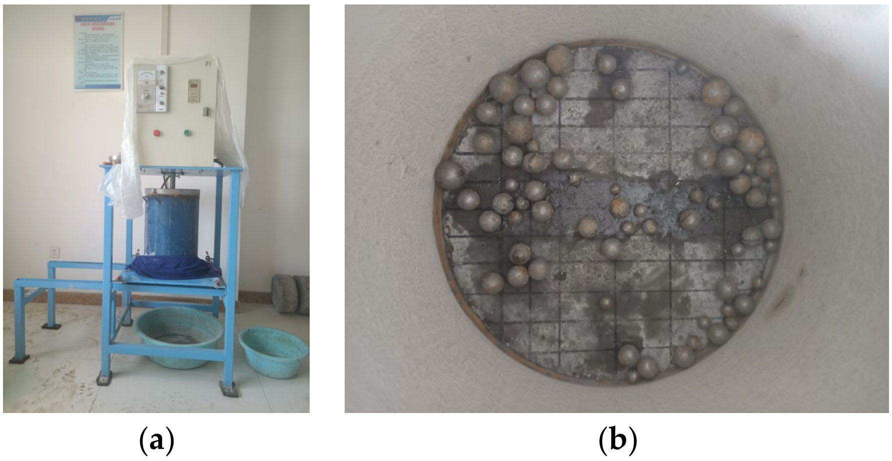

Figure 5. Underwater test: (**a**) HKCM-2 abrasion resistance performance testing machine. (**b**) The placement of steel ball.

2.3.4. The 3D Surface Morphology

In this study, the mechanical probe testing point method was used to compose a simplified 3D surface morphology scanning measurement system test, which can reflect the change in concrete surface morphology characteristics. A three-dimensional Cartesian coordinate system was constructed with the centre of the specimen circle as the centre and the Z-axis aligned vertically with the specimen surface. The depth gauge is used to replace the sensor to test the wear depth of the specimen. The wear morphology of the whole specimen surface can be tested by moving the depth gauge along the X-axis and the moving bracket along the Y-axis, and the distance between adjacent testing points is 5 mm. Based on the test data, the wear depth was shown in Equation (6), and the wear volume was calculated in Equation (7):

$$d_a = \sum_{i=1}^{N} \Delta z / N \tag{6}$$

$$V = \iint_s [Z_0 - Z(X,Y)]dS = \iint_s \Delta Z dS = \sum_{n=1}^{N} \Delta Z_{(X_n,Y_n)} \Delta S_n \tag{7}$$

where S and s are the area of the whole and single testing point of the concrete wear specimen, mm^2, respectively; Δz is the wear depth of each testing point on the surface of the specimen, mm; N is the total number of testing points. When the distance between testing points is 5 mm, N = 2826.

The surface of concrete specimens will form complex sags and crests, perforated multi-scale structures after wear. These structures have self-similarity; that is, they show similar characteristics at different scales. The fractal dimension can be used to quantify this self-similarity. By calculating the fractal dimension of concrete surface, the damage degree of concrete can be quantitatively analysed. The fractal dimension of test specimen surfaces was determined under various working conditions and was calculated by cube covering method. A square mesh *ABCD* is assumed on the worn surface. These four test points correspond to four worn surface altitude values. The number of cubes with side length δ used to cover the ABCD surface is $N_{i,j}$ [31,35,36].

$$N_{i,j} = int\left\{\frac{1}{\delta}\left[max\left(h_{(i,j)}, h_{(i+1,j)}, h_{(i,j+1)}, h_{(i+1,j+1)}\right) - min\left(h_{(i,j)}, h_{(i+1,j)}, h_{(i,j+1)}, h_{(i+1,j+1)}\right)\right] + 1\right\} \tag{8}$$

where *int* is an integral function, and $N(\delta)$ is calculated in Equation (9):

$$N(\delta) = \sum_{i,j=1}^{n-1} N_{i,j} \tag{9}$$

If self-similarity is present on the surface of concrete, then there exists a functional relationship between $N(\delta)$ and δ, as shown in Equation (10):

$$N(\delta) \sim \delta^{-\mathrm{D}} \tag{10}$$

Therefore, the fractal dimension (D) of wearing surface is calculated as in Equation (11):

$$D = -\lim_{\delta \to 0} \frac{lnN(\delta)}{ln(\delta)} \tag{11}$$

3. Results and Discussion

3.1. Mass Loss Rate

The mass loss rate (W_n) of various working conditions in each test cycle was calculated by Equation (1):

$$W_n = \frac{m_0 - m_n}{m_0} \times 100\%, \tag{12}$$

where m_0 and m_n are the weight of initial specimens and the specimen of various working conditions in each test cycle.

The mass loss rates of various working conditions in different test cycles are shown in Figure 6. Figure 6a demonstrates that the mass loss rate of concrete under working condition F group increases slowly with an increase in the number of freeze–thaw cycles. Figure 6b demonstrates that the mass loss rate of concrete under the working condition W group gradually increases with the increased wearing time, and the increase rate is greater than that of the working condition F group. It can be seen from Figure 6c that the mass loss rate of concrete increased significantly with the increase in the number of alternating cycles under the working condition F-W group, compared to the working condition F group and working condition W group. Under the same water/binder ratio, the mass loss rate of the working condition F-W group is higher than the summation of the mass loss rate of the working condition F group and the working condition W group. Additionally, the impact of the working condition F-W group and the working condition W group on the mass loss rate of the specimen is greater than that of the working condition F group. The results show that under the alternating action of freeze–thaw and abrasion, microcracks are generated from the surface to the interior of the concrete, and the surface concrete is easily worn. The new mortar layer and coarse aggregate are exposed on the surface and accompanied by a large number of shedding phenomena, which is the main reason for the mass loss of concrete [37]. During the alternating action of freeze–thaw and abrasion, the crisp skin and pockmarked surface morphology of the concrete surface due to freeze–thaw action become the plastic wear and stress concentration area of abrasion, which aggravates the damaging effect of abrasion [11]. At the same time, a large number of connected cracks are generated between the surface layer and the interior after abrasion, which promotes the further freeze–thaw of concrete [38]. Consequently, the mass loss rate under the F-W group working condition exceeds the combined mass loss rates of the F group and the W group working conditions. Compared with the first three alternating cycles, when the number of alternating cycles of freeze–thaw cycles and abrasion damage reaches four times, the difference between the mass loss rate of the working condition F-W group and the mass loss rate of the working condition F group and working condition W group will reach the maximum. The data show that the difference in the concrete mass loss rate of A3 is 1.92%. The researcher found that the lower the W/B, the smaller the damage degree of concrete under alternating action [39].

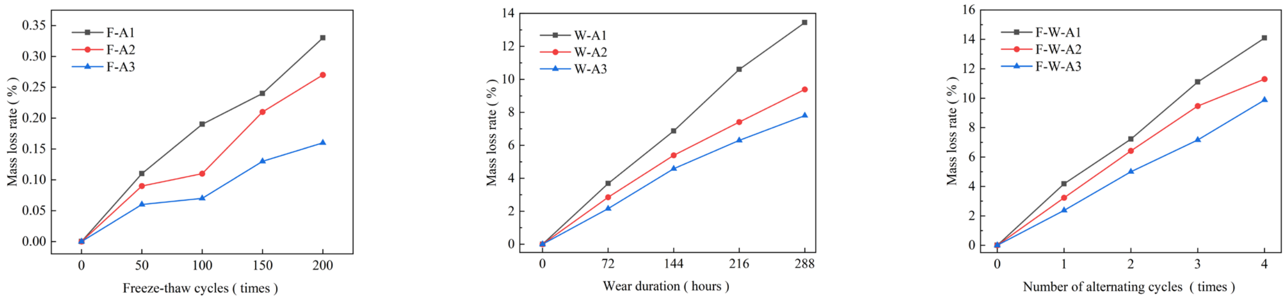

(**a**) (**b**) (**c**)

Figure 6. The mass loss rate variation under various working conditions: (**a**) Working condition F group; (**b**) Working condition W group; (**c**) Working condition F-W group.

3.2. Relative Dynamic Elastic Modulus

The RDEM (E_n) of various working conditions in each test cycle was calculated by Equation (2):

$$E_n = \frac{f_n^2}{f_0^2} \times 100\% \tag{13}$$

where f_0 and f_n are the natural frequency of initial specimens and the specimen of various working conditions in each test cycle.

The RDEM of various working conditions in different test cycles are shown in Figure 7. The RDEM of the working condition F-W group decreases rapidly with an increase in the number of alternating cycles compared to the working condition F group. At the initial stage of F-A3, the freezing of pore water in the specimen slightly increased the density of concrete, and the RDEM slightly increased. However, with the increase in freeze–thaw cycles, the internal pore structure of the specimen deteriorated, and the RDEM began to decrease slowly [40]. The RDEM of the working condition F-W group decreases obviously with the alternating cycles. This is because the holes and cracks after freeze–thaw and the defects such as crisp skin and pockmarked surface on the outer surface are easy to become the plastic wear and stress concentration area during the abrasion damage, which further deepens the degree of abrasion damage and expands the area of abrasion. This, in turn, provides a path for the infiltration of external water along the connected holes and microcracks in the freeze–thaw cycle. The crystallisation pressure of pore water increases, causing damage to the internal structure of concrete, reducing the overall compactness, exacerbating the damage degree of abrasion damage, and significantly reducing the RDEM [6].

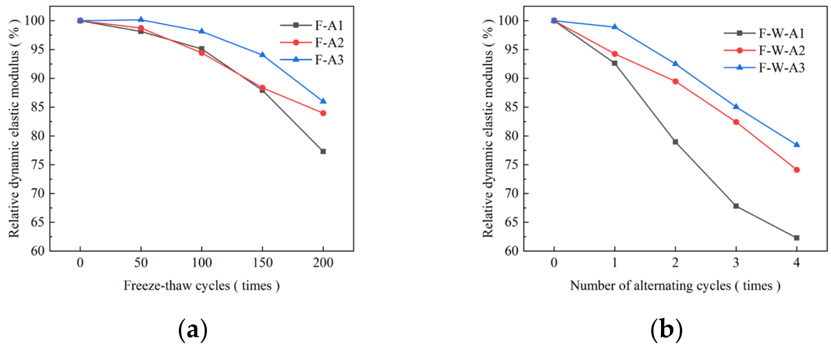

Figure 7. The relative dynamic elastic modulus (RDEM) variation under various working conditions: (**a**) Working condition F group; (**b**) Working condition F-W group.

3.3. The 3D Surface Morphology and Fractal Dimension

3.3.1. The 3D Surface Morphology

Taking the test specimens numbered F-W-A1 and W-A1 as an example, the change process of the 3D surface morphology wear characteristics of concrete specimens under alternating action and abrasion damage is shown in Figures 8 and 9.

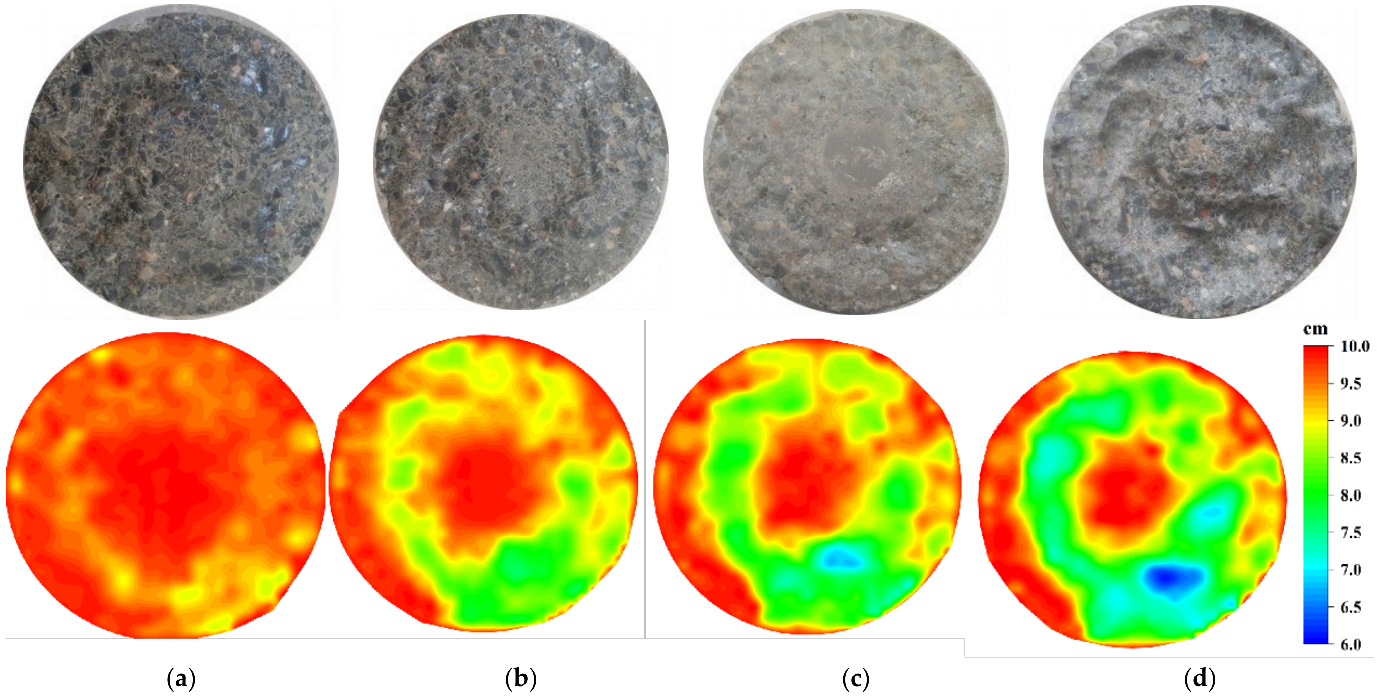

Figure 8. Three-dimensional wear morphology changes of F-W-A1 group concrete specimens: (**a**) the first alternating cycle; (**b**) the second alternating cycle; (**c**) the third alternating cycle; (**d**) the fourth alternating cycle.

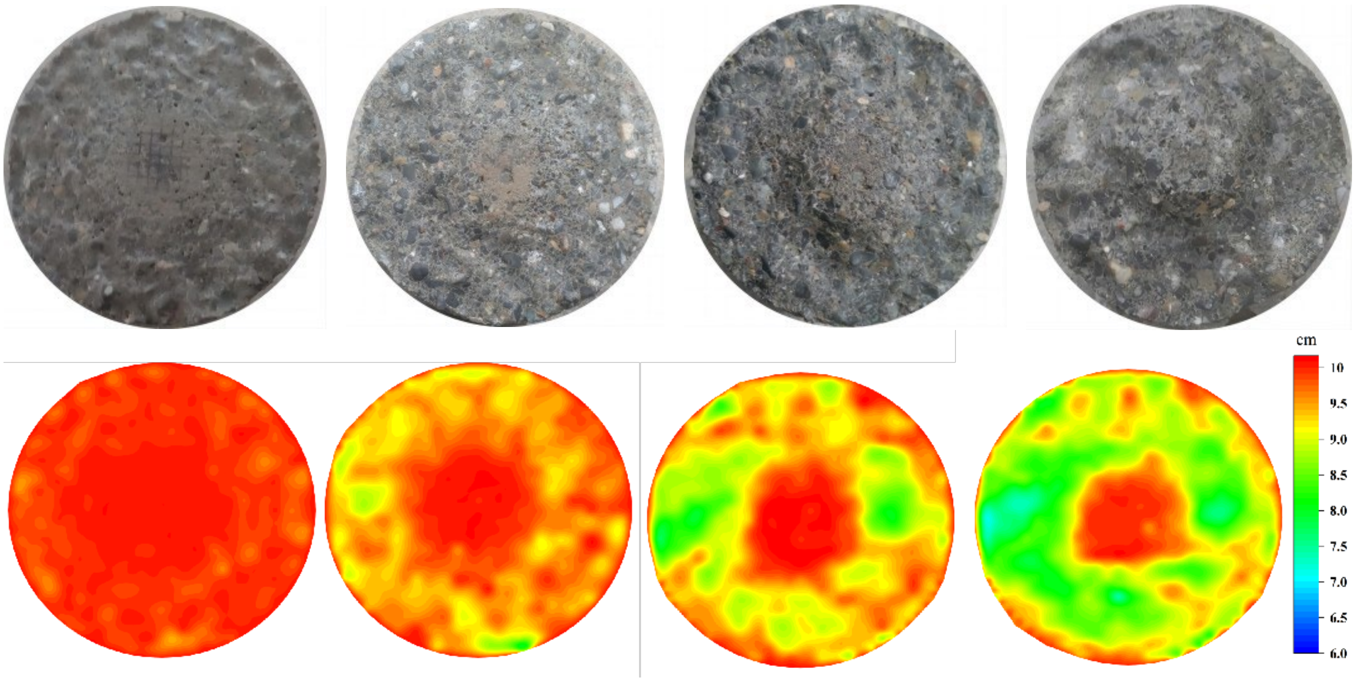

(**a**) (**b**) (**c**) (**d**)

Figure 9. Three-dimensional wear morphology changes of W-A1 group concrete specimens: (**a**) abrasion of 72 h; (**b**) abrasion of 144 h; (**c**) abrasion of 216 h; (**d**) abrasion of 288 h.

As illustrated in Figures 8 and 9, the F-W-A1 group and the W-A1 group showed a consistent development trend under different alternating cycle periods and different wearing times. As the number of alternating cycles and the wearing time increase, the edge and peripheral parts of the samples are initially exposed to abrasion damage, followed by the gradual subjection of the central part of the samples to abrasion damage, which in turn results in a phased decline of the specimen's area. The irregular area between the edge of the samples and the undamaged part of the centre of the samples increased step by step [31]. In the three-dimensional wear morphology chart, we can observe such a phenomenon, where the surface wear of the test specimen is more serious; it is often the part of the test specimen with a higher degree of irregularity. This is because these highly irregular parts are continuously exposed to the environment of high-speed water flow carrying steel balls, and the wearing effect of steel balls becomes more serious over time, which aggravates the negative impact of wear damage on the specimens [41]. On the same abrasion days, the surface wear degree of the F-W-A1 group is more serious than that of the W-A1 group, which indicates that the freeze–thaw cycle accelerates the abrasion damage of the concrete specimen. Specifically, in the alternating action, the temperature difference in the freeze–thaw process causes uneven compression and expansion of the concrete surface layer, resulting in further expansion of the micro-defects in the concrete surface layer. When the wearing is carried out, the bonding capacity of the concrete surface layer is weak, so it is easy to be worn.

3.3.2. Abrasion Depth and Volume Loss

The abrasion depth and volume loss of various working conditions in different test cycles are shown in Figures 10 and 11, respectively. The abrasion depth and volume loss of concrete under each group of working conditions increase with the extension of the test cycle, and the growth rate increased significantly in the second test cycle. It shows that the surface layer of concrete freeze–thaw damage is more prone to abrasion damage, and the alternating action aggravates the abrasion depth and volume loss of concrete. In the same alternating cycle, the abrasion depth and volume loss of concrete in the working condition F-W group are F-W-A1, F-W-A2 and F-W-A3 in descending order. Compared with the concrete of working condition group W with the same wearing time, the abrasion depth of the three after four alternating cycles increased by 23.69%, 39.81%, and 9.78%, and the volume loss increased by 23.9%, 42.45%, and 10.05%.

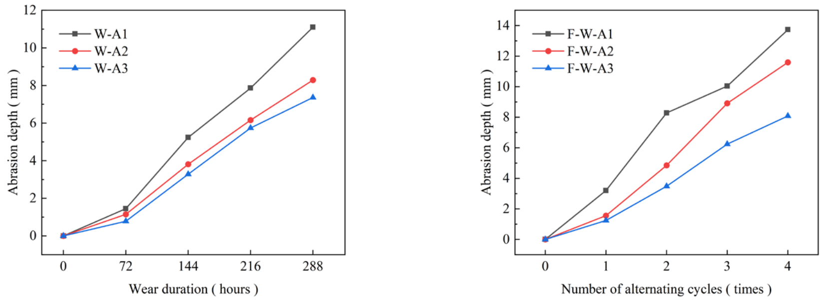

(**a**) (**b**)

Figure 10. The abrasion depth variation under various working conditions: (**a**) Working condition W group; (**b**) Working condition F-W group.

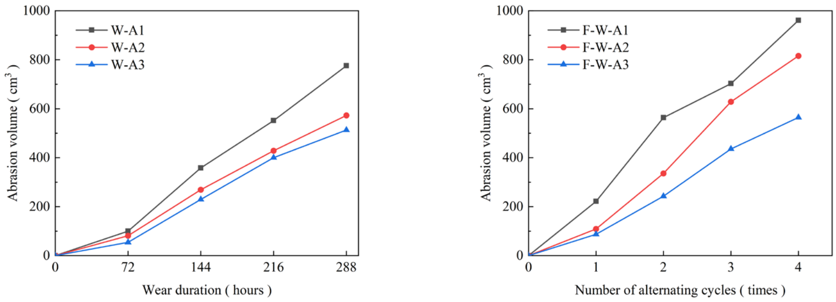

(**a**) (**b**)

Figure 11. The abrasion volume loss variation under various working conditions: (**a**) Working condition W group; (**b**) Working condition F-W group.

3.3.3. Fractal Dimension of Abrasion Surface

The fractal dimensions of various working conditions in different test cycles are shown in Tables 3 and 4, respectively. The data presented in Tables 3 and 4 demonstrate that the fractal dimension of concrete specimens in the working condition F-W and W groups increases with the duration of the test period. However, they did not exceed the limit of 2.4, and this change trend is consistent. Under the same number of alternating cycles, the fractal dimension of the three groups of concrete specimens is F-W-A1, F-W-A2, and F-W-A3 in descending order. At the same abrasion time, the fractal dimension of the F-W group specimens is larger than that of the W group specimens, which also indicates that the freeze–thaw cycle accelerates the abrasion damage of the concrete specimens [42]. The main reason for this phenomenon is that the higher the W/B, the worse the durability of concrete. Compared with the single wearing effect, the surface of the specimen is subjected to greater abrasion damage after alternating action. Therefore, the fractal dimension representing the wear degree of the specimen is also larger.

Table 3. Fractal dimension of Working Condition W group.

Working Condition	Test Specimen Number	Fractal Dimension/D			
		72 h	144 h	216 h	288 h
W	W-A1	2.2959	2.3249	2.3620	2.3819
	W-A2	2.2792	2.3099	2.3428	2.3443
	W-A3	2.1929	2.3033	2.3128	2.3437

Table 4. Fractal dimension of Working Condition F-W group.

Working Condition	Test Specimen Number	Fractal Dimension/D			
		1 Alternating Cycle	2 Alternating Cycles	3 Alternating Cycles	4 Alternating Cycles
F-W	F-W-A1	2.3028	2.3405	2.3708	2.3823
	F-W-A2	2.2880	2.3177	2.3552	2.3740
	F-W-A3	2.2621	2.3094	2.3264	2.3560

The change process of the apparent morphology characteristics of concrete is accompanied by the loss of mass and volume. The fractal dimensions of the working condition F-W group and the working condition W group are linearly fitted with their mass loss rate and volume loss, respectively. The resulting data are presented in Figures 12 and 13. As illustrated in Figures 12 and 13, compared with the working condition W group, the linear fitting effect of the fractal dimension of the working condition F-W group with its mass loss rate and volume loss is more significant, reflecting its strong correlation. With the increase of fractal dimension, its mass loss rate and volume loss are also gradually increasing. By fitting the fractal dimension with the data of mass loss rate and volume loss, respectively, it is found that the alternating action aggravates the wear of concrete. This is due to the fact that the alternating effect is more likely to result in the formation of a complex concrete surface morphology than the wearing effect. Furthermore, its complex fractal structure is more likely to affect the mass and volume loss. Through the linear fitting function of Figures 12b and 13b, the wear mass loss and wear volume loss of concrete under alternating action can be approximately calculated by using the fractal dimension of the wear surface morphology of concrete.

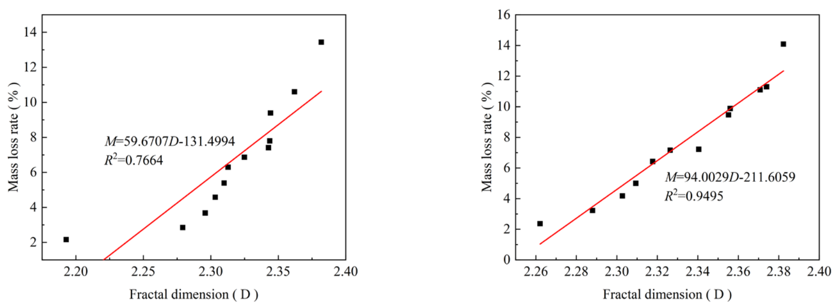

(**a**) (**b**)

Figure 12. The relationship between concrete fractal dimension and mass loss rate under various working conditions: (**a**) Working condition W group; (**b**) Working condition F-W group.

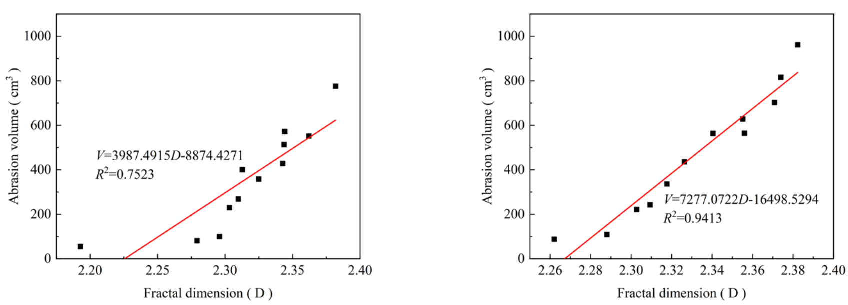

(**a**) (**b**)

Figure 13. The relationship between concrete fractal dimension and volume loss under various working conditions:(**a**) Working condition W group; (**b**) Working condition F-W group.

3.4. Damage Layer Thickness

The surface of the specimen in the working condition F-W group has sags and crests, and the nonmetallic ultrasonic tester cannot be used for testing. Consequently, the damage layer evolution process of the working condition F group was subjected to testing in order to ascertain the extent of damage caused by the freeze–thaw effect on the concrete in each alternating cycle of the working condition F-W group. Please refer to Figure 14 for a detailed illustration of the evolution law of concrete damage layer thickness in working condition F.

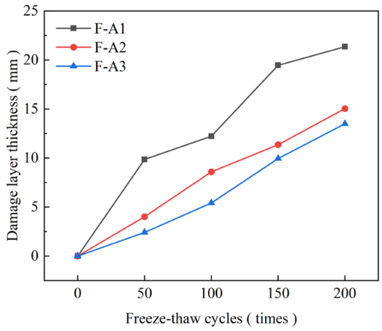

Figure 14. The damage layer thickness variation under working condition F group.

Figure 14 illustrates that the freeze–thaw damage layer of the test specimens, designated F-A1~F-A3, exhibits a varying degree of thickness increase with the number of freeze–thaw cycles. The specimen in the F-A1 group exhibits the most significant change in damage layer thickness. Under the same number of F cycles, the thickness of the freeze–thaw damage layer in the F-A3 group is consistently lower than that of the F-A1 and F-A2 groups. The main reason for this phenomenon is that the lower the W/B, the higher the compactness of the specimen. During the initial stage of the F cycle, the freeze–thaw damage is slight, and the development of pores and cracks is not yet apparent [30]. The tight microstructure can effectively inhibit the expansion of pores and cracks [6]. However, the freeze–thaw damage of concrete began to intensify with the increase of freeze–thaw cycles, causing internal pores and cracks to gradually developed and connected with each other [43]. At this time, the tight microstructure of the F-A3 specimens can still effectively inhibit the development of pores and cracks, thereby reducing freeze–thaw damage [44]. The microstructure of the F-A1 group is less tight than that of the F-A2 and F-A3 groups. This leads to insufficient inhibition of pore and crack development, resulting in an increase in the thickness of the freeze–thaw damage layer. Therefore, the freeze–thaw action on each group of specimens results in the full development of internal pores and cracks, an increase in internal defects, and a significant increase in the thickness of the freeze–thaw damage layer. This has a detrimental effect on the durability of the concrete.

According to the data in Figure 10, the cumulative percentage of concrete abrasion depth increased by alternating action is plotted. Figure 15 illustrates that the three groups of samples show the same law under different alternating cycle times. The freeze–thaw and abrasion effect will cause damage to the concrete from the surface to the interior, increase the penetration path with the internal porosity and micro-cracks of the specimen, and destroy the integrity of the specimen. The measurement results indicate that controlling the W/B can reduce freeze–thaw damage and abrasion depth of the concrete surface layer. It has been found that a lower water/binder ratio results in less damage to the concrete surface caused by freeze–thaw action, as well as a smaller increase in the abrasion depth of samples under alternating action. The reason is that the pore water in concrete causes micro-level damage during the F cycles. However, the layer of damage caused by freeze–thaw still maintains a high adhesive strength, which preserves the integrity of the specimen.

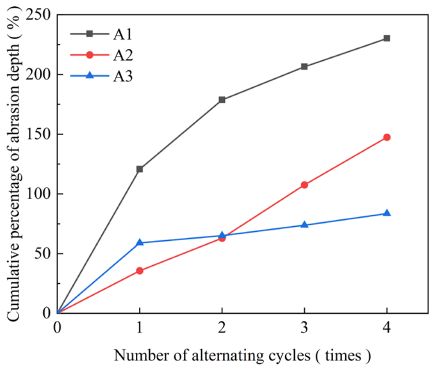

Figure 15. Cumulative percentage of concrete abrasion depth increased by alternating action.

4. Innovations and Deficiencies

4.1. Innovation

The evolution process of hydraulic concrete performance under the action of freeze–thaw and abrasion is revealed from the macroscopic scale. The three-dimensional morphology and fractal dimension are introduced to analyse the morphological characteristics of the surface of hydraulic concrete.

4.2. Deficiencies

The size of the standard specimen of freeze–thaw and abrasion is inconsistent. In this test, the standard-size specimen of anti-abrasion is used instead of the standard frost-resistant specimen for the alternate test. This method may not conform to the test specification, but this concept can be extended to the actual scene; hydraulic concrete, regardless of shape, will suffer from adverse effects from the outside world.

5. Conclusions

In this paper, the mass loss rate, RDEM, and damage layer thickness of samples under various working conditions are tested. The macroscopic deterioration behaviour characteristics under the alternating action of F and W were studied. The effects of alternating action on the apparent morphology characteristics of concrete and its fractal dimension were compared and analysed. The main conclusions are as list follows:

(1) During the initial stages of the alternating action of F and W, the surface layer of samples develops a crispy skin and pockmarked form due to F action. It becomes the area of plastic wear and stress concentration, which aggravates the damaging effect of wearing. This, in turn, provides an infiltration path for external water along the connecting pores and microcracks during freeze–thaw action. The internal structure of the concrete was damaged due to increased pore water crystallisation pressure, leading to a decrease in overall compactness. The alternating action accelerates the mass loss of concrete and reduces the RDEM. The maximum difference in mass loss rate and RDEM of concrete between the control and experimental groups was 1.92% and 20.11%, respectively.

(2) With the increased alternating cycle period and wearing time, the change in apparent morphology characteristics of concrete shows a consistent development trend. The damage of the central part of the specimen increases gradually, while the proportion of the ring area between the undamaged part and the edge of the specimen increases. However, the F action accelerates the abrasion damage of the specimen, while the surface wear in the F-W group under operational conditions is more pronounced.

(3) The fractal dimension of the sample increases with the increase of the test period. However, it did not exceed the limit of 2.4. It was found that the linear correlation between the fractal dimension, the mass loss rate, and the volume loss of the working condition F-W group was higher than that of the working condition W group, and it can be concluded that the alternating action exacerbated the damage to the concrete.

The results showed that the experimental group had a good linear correlation; the correlation was close to 95%, and the control group was about 75%.

(4) The tightness of low W/B concrete is stronger, so it has a stronger performance in inhibiting the development of pores and cracks. The freeze–thaw damage layer generated under freeze-thaw action still maintains high adhesive strength, reduces the wear depth of concrete under alternating action, and maintains the integrity of the whole concrete.

Author Contributions: S.L.: Conceptualisation, funding acquisition, methodology, project administration, resources, supervision. B.W.: Data curation, formal analysis, investigation, validation, writing—original draft. C.J.: Visualisation, writing—review and editing. All authors have read and agreed to the published version of the manuscript.

Funding: We acknowledge the National Natural Science Foundation of China, China (under Grant No. 52269028) and the Natural Science Foundation of Xinjiang Uygur Autonomous Region (2022D01B104).

Data Availability Statement: The data in the paper are measured in individual experiments and are not publicly available.

Conflicts of Interest: The authors declare no conflicts of interest.

References

1. Sharp, J.H. Surely we know all about cement—Don't we? *Adv. Appl. Ceram.* **2006**, *105*, 162–174. [CrossRef]
2. Ma, R.; Cui, C.; Ma, M.; Chen, A. Performance-based design of bridge structures under vehicle-induced fire accidents: Basic framework and a case study. *Eng. Struct.* **2019**, *197*, 109390. [CrossRef]
3. Lu, P.; Shi, Q.; Ye, K.; Wu, Y.; Lu, L.; Zhou, Y. Prediction of mechanical behavior of reinforced concrete bridges following a fire based on the fire dynamics simulator–kriging model. *Struct. Concr.* **2023**, *24*, 5855–5871. [CrossRef]
4. Alomari, Q.; Linzell, D. Reinforced Concrete Bridge Column Multihazard Performance: A Computational Tool to Assess Response to Vehicle Impact, Air Blast, and Fire. *J. Perform. Constr. Fac.* **2024**, *38*, 04023061. [CrossRef]
5. Peng, X.; Zhou, M. Thermo-mechanical behavior of composite beams with corrugated steel webs exposed to localized fire. *J. Constr. Steel Res.* **2023**, *211*, 108180. [CrossRef]
6. Zhu, X.; Bai, Y.; Chen, X.; Tian, Z.; Ning, Y. Evaluation and prediction on abrasion resistance of hydraulic concrete after exposure to different freeze-thaw cycles. *Constr. Build. Mater.* **2022**, *316*, 126055. [CrossRef]
7. Yu, W.; Zhang, T.; Lu, Y.; Han, F.; Zhou, Y.; Hu, D. Engineering risk analysis in cold regions: State of the art and perspectives. *Cold Reg. Sci. Technol.* **2020**, *171*, 102963. [CrossRef]
8. Doelhomid, S. Sediment control of the brantas river. *Water Int.* **1982**, *7*, 123–126. [CrossRef]
9. Gong, J.; Qin, C.; Tang, X.; Zhang, T. Experimental study and field application of abrasion resistance for the repair of concrete water-conveying structures. *Mater. Struct.* **2022**, *55*, 167. [CrossRef]
10. Su, X.; Wang, L.; Liu, W.; Wang, R.; Li, Y. Deterioration of interfacial bonding performance between metal mortar and concrete under the coupling effect of freeze-thaw cycle and abrasion. *J. Build. Eng.* **2024**, *85*, 108628. [CrossRef]
11. Liu, M.; Han, B.; Ma, J. Research on the anti-abrasion capacity of concrete under freeze-thaw cycle. *China Civ. Eng. J.* **2019**, *52*, 100–109. (In Chinese)
12. Tian, W.; Gao, F. Damage and degradation of concrete under coupling action of freeze-thaw cycle and sulfate attack. *Adv. Mater. Sci. Eng.* **2020**, *2020*, 8032849. [CrossRef]
13. Lee, M.; Wang, Y.; Wang, W.; Hsieh, Y. Abrasion and Maintenance of High-Strength Fiber-Reinforced Pervious Concrete. *Buildings* **2024**, *14*, 127. [CrossRef]
14. Lee, M.; Wang, Y.; Wang, W.; Chien, H.; Cheng, L. Experimental Study on the Mechanical Properties of Reinforced Pervious Concrete. *Buildings* **2023**, *13*, 2880. [CrossRef]
15. Tan, K.; Zhang, T.; Zhu, W.; Yang, D.; Lin, D.; Wang, H.; Wei, J.; Yu, Q. Innovative High-Strength, High-Permeability Concrete for Large-Scale Applications in Permeable Subgrade of Highway Tunnel. *Case Stud. Constr. Mater.* **2024**, *20*, e02977. [CrossRef]
16. Long, X.; Tan, Y.; Wan, X.; Zhou, L.; Wang, C. Effect of freeze-thaw cycles and chloride salt erosion coupling conditions on fatigue properties of PE-ECC. *Case Stud. Constr. Mater.* **2024**, *20*, e02726. [CrossRef]
17. Xiao, Q.; Cao, Z.; Guan, X.; Li, Q.; Liu, X. Damage to recycled concrete with different aggregate substitution rates from the coupled action of freeze-thaw cycles and sulfate attack. *Constr. Build. Mater.* **2019**, *221*, 74–83. [CrossRef]
18. Omran, H.Y.; El-Hacha, R. Effects of sustained load and freeze-thaw exposure on RC beams strengthened with prestressed NSM-CFRP strips. *Adv. Struct. Eng.* **2014**, *17*, 1801–1816. [CrossRef]
19. Cao, D.; Qin, X.; Meng, S.; Tu, Y.; Elfgren, L.; Sabourova, N.; Grip, N.; Ohlsson, U.; Blanksvärd, T. Evaluation of prestress losses in prestressed concrete specimens subjected to freeze–thaw cycles. *Struct. Infrastruct. Eng.* **2016**, *12*, 159–170. [CrossRef]
20. Wang, X.; Petrů, M. Mode I fracture evaluation of CFRP-to-concrete interfaces subject to aggressive environments agents: Freeze-thaw cycles, acid and alkaline solution. *Compos. Part B Eng.* **2019**, *168*, 581–588. [CrossRef]

21. Fu, Q.; Bu, M.; Zhang, Z.; He, J.; Li, D.; Xu, W.; Niu, D. Chloride ion transport performance of lining concrete under coupling the action of flowing groundwater and loading. *Cem. Concr. Compos.* **2021**, *123*, 104166. [CrossRef]
22. Huovinen, S. Abrasion of concrete by ice in arctic sea structures. *Nord. Concr. Res.* **1989**, *8*, 103–115.
23. Huovinen, S. Abrasion of concrete structures by ice. *Cem. Concr. Res.* **1993**, *23*, 69–82. [CrossRef]
24. Jacobsen, S.; Scherer, G.W.; Schulson, E.M. Concrete-ice abrasion mechanics. *Cem. Concr. Res.* **2015**, *73*, 79–95. [CrossRef]
25. Guo, T.; Weng, X. Evaluation of the freeze-thaw durability of surface-treated airport pavement concrete under adverse conditions. *Constr. Build. Mater.* **2019**, *206*, 519–530. [CrossRef]
26. Liu, Q.; Li, L.; Andersen, L.V.; Wu, M. Studying the abrasion damage of concrete for hydraulic structures under various flow conditions. *Cem. Concr. Compos.* **2023**, *135*, 104849. [CrossRef]
27. Hasan, M.S.; Li, S.S.; Zsaki, A.M.; Nokken, M.R. Measurement of abrasion on concrete surfaces with 3D scanning technology. *J. Mater. Civil. Eng.* **2019**, *31*, 04019207. [CrossRef]
28. Sarker, M.; Dias-da-Costa, D.; Hadigheh, S.A. Multi-scale 3D roughness quantification of concrete interfaces and pavement surfaces with a single-camera set-up. *Constr. Build. Mater.* **2019**, *222*, 511–521. [CrossRef]
29. *SL/T 352—2020*; Text Code for Hydraulic Concrete. China Conservancy and Hydropower Press: Beijing, China, 2020. (In Chinese)
30. Bai, Y.; Ye, X.; Liu, H.; Lu, L.; Ning, F.; Zhange, F. Concrete damage process under the coupling action of freeze-thaw cycle and water flow. *Ewrhi* **2019**, *40*, 64–69. (In Chinese)
31. Jiang, C.; Jiang, L.; Chen, C.; Gong, J.; Li, S. Evaluation and prediction on the hydraulic abrasion performance of high belite cement-based concrete. *KSCE J. Civ. Eng.* **2021**, *25*, 2175–2185. [CrossRef]
32. *CECS 201-2000*; Technical Specification for Ultrasonic Detection of Concrete Defects. Standards Press of China: Beijing, China, 2000. (In Chinese)
33. Fu, Q.; Bu, M.; Li, D.; Xu, W.; He, J.; Niu, D. Resistance to sulfate attack and chemo-damage-transport model of sulfate ions for tunnel lining concrete under the action of loading and flowing groundwater. *ACS Sustain. Chem. Eng.* **2021**, *9*, 14307–14326. [CrossRef]
34. *ASTM C1138*; Standard Test Method for Abrasion Resistance of Concrete (Underwater Method). ASTM International: West Conshohocken, PA, USA, 2012.
35. Jiang, C.; Gong, J.; Jiang, L.; Chen, C.; Tang, X. Research on time-varying behavior and its influence factors of low heat concrete under abrasion. *Mater. Rep.* **2023**, *37*, 155–160. (In Chinese)
36. Su, S.; Hou, P.; Gao, F.; Gao, Y.; Cai, C.; Zhang, Z.; Liang, X. A fractal perspective on structural damage and fracture characteristics of coal subjected to liquid nitrogen cooling at laboratory-scale. *Fractals* **2022**, *30*, 2250080. [CrossRef]
37. Liu, W.; Lin, Y.; Zhong, H.; Su, H. Anti-abrasion test of erosion and denudation resistant concrete. *Eng. Mech.* **2011**, *28*, 157–160.
38. Liu, J.; Lu, L.; Zhang, Z. Mechanism of concrete pavement subjected simultaneously to freeze-thaw and abrasion action. *Concrete* **2008**, *9*, 7–10. (In Chinese)
39. Wu, F.; Chen, X.; Chen, J. Abrasion resistance of concrete under coupled debris flow and freeze-thaw cycles. *Wear* **2023**, *524*, 204805. [CrossRef]
40. Zhang, K.; Zhou, J.; Yin, Z. Experimental study on mechanical properties and pore structure deterioration of concrete under freeze-thaw cycles. *Materials* **2021**, *14*, 6568. [CrossRef] [PubMed]
41. Choi, S.; Bolander, J. A topology measurement method examining hydraulic abrasion of high workability concrete. *KSCE J. Civ. Eng.* **2012**, *16*, 771–778. [CrossRef]
42. Ismail, M.; Hassan, A. Abrasion and impact resistance of concrete before and after exposure to freezing and thawing cycles. *Constr. Build. Mater.* **2019**, *215*, 849–861. [CrossRef]
43. Zhang, J.; Deng, H.; Taheri, A.; Ke, B.; Liu, C.; Yang, X. Degradation of physical and mechanical properties of sandstone subjected to freeze-thaw cycles and chemical erosion. *Cold Reg. Sci. Technol.* **2018**, *155*, 37–46. [CrossRef]
44. Wu, F.; Chen, X.; Li, X. Abrasion performance of cement mortar by debris flow. *Tribol. Int.* **2022**, *175*, 107839. [CrossRef]